High Frame Rate Echocardiography for Detailed Analysis of Cardiac Dynamics

Hideyuki Hasegawa[1,2] and Hiroshi Kanai[2,1]

1 Graduate School of Biomedical Engineering, Tohoku University
2 Graduate School of Engineering, Tohoku University
E-mail: hasegawa@ecei.tohoku.ac.jp, hkanai@ecei.tohoku.ac.jp

Abstract

Echocardiography is a widely-used modality for diagnosis of the heart. It enables observation of the shape of a heart and estimation of global heart function based on B-mode and M-mode imaging. Subsequently, methods for estimating myocardial strain and strain rate have been developed to evaluate regional heart function. Furthermore, it has been recently shown that measurements of transmural transition of myocardial contraction/relaxation and propagation of vibration caused by closure of a heart valve would be useful for evaluation of myocardial function and viscoelasticity. However, such measurements require a frame rate much higher than that achieved by conventional ultrasonic diagnostic equipment. In the present study, a method based on parallel receive beamforming was developed to achieve high-frame-rate echocardiography over 300 Hz. To increase the frame rate, the number of transmits was reduced to 15 with angular intervals of 6 degrees, and 16 receiving beams were created for each transmission to obtain the number and density of scan lines which were same as those realized by conventional sector scanning. In addition, several transmits were compounded to obtain each scan line to reduce the differences in transmit-receive sensitivities among scan lines. The number of transmits for compounding was determined by considering the width of the transmit beam. For transmission, plane waves and diverging waves were investigated. Diverging waves showed better performance than plane waves because the widths of plane waves did not increase with the range distance from an ultrasonic probe, whereas lateral intervals of scan lines increased with range distance. The spatial resolution of the proposed method was validated using fine nylon wires. Although the widths at half maxima of the point spread functions obtained by diverging waves were slightly larger than those obtained by conventional beamforming and parallel beamforming with plane waves, the point spread functions, which were very similar to that obtained by conventional beamforming could be realized by parallel beamforming with diverging beams and compounding. However, there was an increase in the lateral sidelobe level in the case of parallel beamforming with plane and diverging waves. Furthermore, a heart of a 23-year-old healthy male was measured. Although contrast of the B-mode image obtained by the proposed method was degraded due to the increased sidelobe level, a frame rate of 316 Hz, which was much higher than that realized by conventional sector scanning of several tens of Hertz, was realized with a full lateral field of view of 90 degrees.

1. Introduction

Echocardiography is one of the predominant modalities for the diagnosis of the heart because it provides a cross-sectional image of the heart noninvasively in real time. Owing to the high temporal resolution of ultrasonic diagnostic equipment, global heart function, such as ejection fraction (EF), can be estimated based on B-mode and M-mode imaging much more easily compared with other diagnostic modalities, such as magnetic resonance imaging (MRI) and computed tomography (CT). To evaluate regional myocardial function quantitatively, methods for measurements of myocardial strain and strain rate have been developed [1-3]. These methods enable estimation of regional deformation of the heart wall based on measurements of movement. Although measured strain and strain rate themselves are useful for evaluation of the regional myocardial function, it has recently been shown that the measurements of transmural transition of myocardial contraction/relaxation and propagation of vibration caused by closure of a heart valve would be useful for evaluation of myocardial function and viscoelasticity [4-6]. However, such measurements require a frame rate much higher than that achieved by conventional ultrasonic diagnostic equipment. For example, electrical excitation propagates in Purkinje fibers and ventricular muscle at typical velocities of 0.3 to 4 m/s [7], and the corresponding propagation velocities of myocardial contraction of 0.5 to 7 m/s were measured by ultrasound [5,8]. A high frame rate, typically higher than 200 Hz, which is much higher than that realized by conventional ultrasonic diagnostic equipment of several tens of Hertz, is required to measure the propagation of this electromechanical wave and the resulting transient small motion of the heart wall.

Konofagou et al. [9] and D'hooge et al.[10] increased the frame rate to above 200 Hz by reducing the size of the field of view and the total number of scan lines in an ultrasonic image. Furthermore, Konofagou et al. introduced a electrocardiogram (ECG)-gating technique in ultrasound imaging to

combine individual small sectors into a large field of view [11]. In this method, the lateral size of a sector (corresponding to the number of scan lines), which is obtained in one acquisition, is narrowed to achieve a higher frame rate of about 500 Hz. By measuring a number of small sectors during the corresponding number of cardiac cycles, the measured small sectors are combined into a large sector format based on ECG-gating. Although this method achieves a frame rate of about 500 Hz, which is much higher than the conventional frame rate of several tens of Hertz, measurements for a number of cardiac cycles are required.

To achieve a high frame rate of about 500 Hz without ECG-gating, we used sparse sector scanning, in which the number of scan lines was decreased to about 10 [12]. In this method, the angle intervals between scan lines are increased to obtain a large lateral field of view with a small number of scan lines. Therefore, the lateral image resolution is significantly degraded.

The above-mentioned methods are based on conventional beamforming. Therefore, they need to sacrifice the density of scan lines or field of view to achieve a high frame rate. To overcome this problem, parallel receive beamforming with a wide transmit beam have been developed13) to illuminate a wider region by one transmission to reduce the number of transmissions. This could be done in the cited study by conventional transmit beamforming (focusing at a certain range distance) because such beams are wide in the region shallower than the focal distance (between the transducer surface and the focal point). Using this method, real-time 3D imaging of the heart was realized at a frame rate of a few tens of Hertzes. However, the width of the transmit beam is narrower than the size of an aperture, and this would limit the number of receiving beams created by one transmission.

Lu et al. proposed an alternative imaging method using unfocused but non-diverging transmit beam, namely, limited diffraction beam [14-17]. Unfocused beams achieved a wider beam width, and non-diverging beams used in these cited studies prevent the insonified energy from being spread to assure the required penetration depth. However, the width of a non-diverging beam is still limited by the size of an aperture.

On the other hand, diverging beams have potential to enlarge the region illuminated by one transmission. In synthetic aperture ultrasound imaging, a single element or a small number of elements are used to produce spherical waves [21,22]. Although a spherical wave can illuminate a wide area by one transmission, acoustic pressure significantly decreases with propagation distance, and the signal-to-noise ratio (SNR) of the received signal would be significantly reduced.

In the present study, the feasibility of a diverging transmit beam in ultrasonic imaging with parallel beamforming [18-20] was investigated to achieve a frame rate above 200 Hz with an adequate lateral spatial resolution, a wider field of view, and no ECG-gating. Diverging waves can be produced by using all transducer elements in an ultrasonic array probe to obtain ultrasonic echoes with better SNR.23) The width of diverging angle was limited to suppress the decay of acoustic pressure due to the propagation distance. Furthermore, the diverging beam was steered to obtain an ultrasonic image of a heart with a full angle of 90 degrees with a limited beam width. To increase the frame rate, the number of transmits was reduced to 15 with a transmit angular interval of 6 degrees, and 16 receiving beams were created in each transmit to obtain the number and density of scan lines which were same as those realized by conventional sector scanning. The spatial resolution of the proposed imaging method was evaluated by basic experiments using fine nylon wires. Furthermore, B-mode images of a heart of a 23-year-old healthy male measured by the proposed method were obtained.

2. Materials and Methods
2.1. Mathematical description of ultrasound waves emitted from transducer elements

Let us describe ultrasound waves emitted from transducer elements of a phased array ultrasonic probe. To achieve a frame rate over 200 Hz under a typical pulse repetition frequency of 5 kHz (realized by the ultrasound system used in the present study under a setting of an observation range of 130 mm), the number of transmits should be less than 25. Therefore, in the present study, plane waves or diverging waves were transmitted in 15 directions $\{m\Theta\}$ ($m = -7, -6, \cdot\cdot\cdot, 0, 1, \cdot\cdot\cdot, 7$) with angular intervals of $\Theta = 6$ degrees. The ultrasonic wave $g_{i,m}(\mathbf{p}; t)$ at time t from the time of transmission, which is emitted from the i-th transducer element ($i = 0, 1, \cdot\cdot\cdot, L-1$) in the m-th transmission and insonifies to a spatial point p = (r, θ), as shown in Fig. 1, is expressed as follows:

$$g_{i,m}(\mathbf{p}; t) = s_i\left(t - \tau_{\mathrm{t},i,m}(\mathbf{p})\right), \qquad (2.1)$$

where $s_i(t)$ is the impulse response of the i-th transducer element, and $\tau_{\mathrm{t},i,m}(\mathbf{p})$ is a time delay due to propagation of an ultrasonic wave from the i-th element to the spatial point $\mathbf{p}$. The time delay $\tau_{\mathrm{t},i,m}(\mathbf{p})$ of $g_{i,m}(\mathbf{p}; t)$ is given by

$$\tau_{\mathrm{t},i,m}(\mathbf{p}) = \frac{\sqrt{r^2\cos^2\theta + \left\{r\sin\theta - \left(i - \frac{L-1}{2}\right)\Delta x\right\}^2}}{c_0} + T_{\mathrm{TBF},i,m}, \quad (2.2)$$

where Δx and c_0 are the lateral pitch of transducer elements and speed of sound, respectively, and $T_{\mathrm{TBF},i}$ is the time delay applied to the i-th element by the transmit beamformer.

To emit a plane wave at the steering angle of $m\Theta$, $T_{\mathrm{TBF},i,m}$ should be given by

$$T_{TBF,i,m} = \begin{cases} \dfrac{i\cdot\Delta x\cdot\sin(m\Theta)}{c_0} & if\ m \geq 0, \\ \dfrac{(i-L+1)\cdot\Delta x\cdot\sin(m\Theta)}{c_0} & if\ m < 0. \end{cases} \qquad (2.3)$$
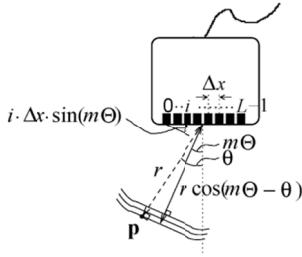
$$(\ i = 0, 1, ..., L\text{-}1)$$

Fig. 1. Illustrations of a plane wave insonifying to spatial point $\mathbf{p} = (r, \theta)$ and propagation distance $r \cos(m\Theta - \theta)$ required to illuminate spatial point $\mathbf{p}$, which is located at distance r from the center of array, using a plane wave.

The time delay $T_{\text{TBF},i,m}$ applied by transmit beamformer is greater than or equal to zero.

For a circular planar transducer, the Fresnel zone (range of near field) is defined by the diameter of the aperture D and ultrasonic wavelength λ as $D^2/(4\lambda)$. The aperture width D of the sector probe and the ultrasonic wavelength λ used in the present study were about 20 mm and about 0.4 mm (center frequency: 3.75 MHz), respectively. Although the phased array probe used in the present study was not circular, the range of near field can be approximately obtained based on this equation. The range of the Fresnel zone of the probe used was 250 mm and, thus, the range of about 130 mm, which was imaged in the present study, was included in the near field. In the near field, the width of a plane wave is constant. On the other hand, in ultrasonic imaging in a sector format, the lateral width of a small sector imaged by one transmission increases with range distance and, thus, the performance of a plane wave would be limited because the lateral width of a plane wave does not increase with range distance in the near field.

To solve this problem, in the present study, a diverging wave, which is illustrated in Fig. 2(a), was used for transmission in addition to a plane wave. In synthetic aperture imaging, each single element is individually used to emit a spherical wave. Such diverging waves would be useful for ultrasonic imaging in a sector format. However, the intensity of the emitted wave would significantly decrease because a single element is used. Alternatively, spherically diverging waves [22] can be produced using all the transducer elements in every transmission. In the present study, such a diverging wave was realized by applying time delay $T_{\text{TBF},i,m}$ to the i-th transducer element in the m-th transmission, which is given by

$$T_{\text{TBF},i,m} =$$
$$\begin{cases} \dfrac{i \cdot \Delta x \cdot \sin(m\Theta)}{c_0} + \dfrac{\sqrt{\left\{\left(i-\frac{L-1}{2}\Delta x\right)\right\}^2 + r_f^2} - r_f}{c_0} & \text{if } m \geq 0, \\[4mm] \dfrac{(i-L+1) \cdot \Delta x \cdot \sin(m\Theta)}{c_0} + \dfrac{\sqrt{\left\{\left(i-\frac{L-1}{2}\right)\right\}^2 + r_f^2} - r_f}{c_0} & \text{if } m < 0, \end{cases}$$
$$(2.4)$$

where r_f is the distance from a virtual point source O_v behind the array to the surface of the transducer array. The first term in the right-hand side of eq. (2.4) is

required to steer the direction of the transmit beam to $m\Theta$. The second term, which is required to realize a diverging wave, was obtained in the present study by considering the geometry illustrated in Fig. 2(b). The second term depends on the distance from the virtual point source O_v to the i-th element in Fig. 2(b).
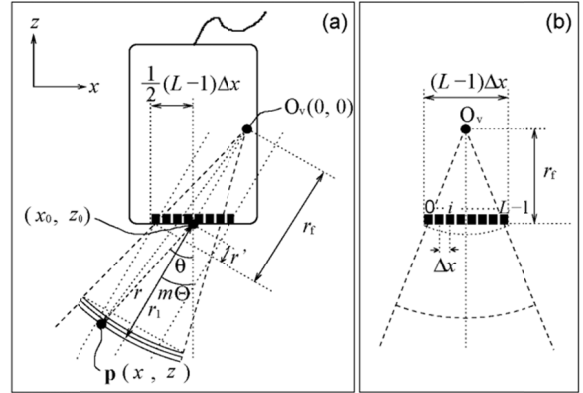

Fig. 2. Illustration of a diverging wave. (a) Propagation distance r1 required to illuminate spatial point p, which is located at distance r from the center of array, using a diverging wave. (b) Geometry for consideration of time delays applied to transducer elements for transmission of diverging wave.

2.2. Parallel receive beamforming

In this study, ultrasonic beams (plane or diverging waves) emitted in 15 directions an angle intervals of $\Theta = 6$ degrees and 16 receiving beams with angle intervals of 0.375 degrees were created for each transmit to realize the number and density of scan lines which are similar to that obtained by conventional sector scanning. The value, $\hat{O}_m(\mathbf{p})$, of the beamformed RF signal at a spatial point $\mathbf{p}$ is generated from ultrasonic echo signals $\{y_{i,m}(t)\}$ received by the elements ($i = 0, 1, ..., L - 1$), which contain echoes scattered at all points illuminated by the m-th transmission, as follows:

$$\hat{O}_m(\mathbf{p}) = \sum_{i=0}^{L-1} w_{r,i} \cdot y_{i,m}\left(t - \tau_{\text{RBF},i,m}(\mathbf{p})\right), \quad (2.5)$$

where $w_{r,i}$ ($i = 0, 1, \cdots, L - 1$) corresponds to the receive apodization, and $\tau_{\text{RBF},i,m}(\mathbf{p})$ is the time delay which should be applied by a receive beamformer to compensate the propagation delay of the emitted wave from the probe to $\mathbf{p}$ and that of the scattered wave from $\mathbf{p}$ to the i-th element. The time delay $\tau_{\text{RBF},i,m}(\mathbf{p})$, which was applied by the receive beamformer to echo signal $y_{i,m}(t)$ received by the i-th element, is given by

$$\tau_{\text{RBF},i,m}(\mathbf{p}) = T_{\text{TW},m}(\mathbf{p}) + \frac{\sqrt{r^2\cos^2\theta + \left\{r\sin\theta - \Delta x\left(i-\frac{L-1}{2}\right)\right\}^2}}{c_0}.$$
$$(2.6)$$

The second term of eq. (2.6) corresponds to the time delay of a scattered echo from the spatial point p to the i-th element. The first term, $T_{\text{TW},m}(\mathbf{p})$, of eq. (2.6) corresponds to the propagation delay of the emitted

ultrasonic wave to spatial point **p** which depends on the receiving beam angle θ. In the present study, as illustrated in Fig. 1, for a plane wave, $T_{\text{TW},m}(\mathbf{p})$ was assigned as follows:

$$T_{\text{TW},m}(\mathbf{p}) = \frac{r\cos(\theta - m\Theta)}{c_0}. \tag{2.7}$$

For diverging waves, as illustrated in Fig. 2(b), $T_{\text{TW},m}(\mathbf{p})$ was assigned as follows:

$$T_{\text{TW},m}(\mathbf{p}) = \frac{\sqrt{x^2 + z^2} - r_f + r'}{c_0}, \tag{2.8}$$

$$x = r_f \sin(m\Theta) - r'\sin(m\Theta) + r\sin\theta, \tag{2.9}$$

$$z = -r_f \cos(m\Theta) + r'\cos(m\Theta) - r\cos\theta, \tag{2.10}$$

$$\mathrm{r}' = \tfrac{1}{2} \cdot (L-1) \cdot \Delta x \cdot \sin(m\Theta), \tag{2.11}$$

where (x, z) is the position of **p** in the Cartesian coordinate.

By changing θ $((m-0.5)\cdot\Theta \leq \theta < (m+0.5)\cdot\Theta)$ at intervals of 0.375 degrees at each range position r in each of the m transmissions, beamformed RF signals $\{\hat{O}_m(\mathbf{p})\}$ at all spatial points $\{\mathbf{p} = (r, \theta)\}$ in the field of view are obtained.
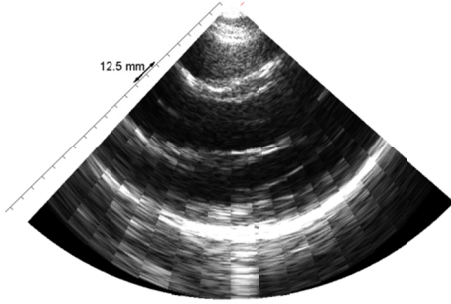

Fig. 3. Longitudinal B-mode image of a heart of a 23-year-old male obtained by parallel beamforming without spatial compounding.

2.3. Problem in parallel beamforming with phased array

To obtain an ultrasonic image in a sector format, ultrasonic beams need to be steered. Therefore, the directivity of the ultrasound beam changes depending on the steering angle. In receive beamforming, the difference between the directivities of neighboring receiving beams is not so significant because the angle intervals of receiving beams are small (0.375 degrees). However, such difference is significant in transmission because of a relatively large angle interval of neighboring transmit beams of 6 degrees (used in the present study). This significant change in directivity in transmission produce discontinuities in a resultant ultrasonic image at a pitch of 6 degrees, which corresponds to angular intervals of transmit beams because the transmit-receive directivity is defined by the product of the transmit and receive directivities [24]. Figure 3 shows a B-mode image of the heart of a 23-year-old healthy male, which was obtained using parallel beam forming expressed by eq. (2.5) with plane wave transmission. As can be seen in Fig. 3, there are significant discontinuities at the edges of each region imaged by one transmission.

2.3. Spatial compound of multiple transmits in receive beamforming

As described in the previous section, there are discontinuities in an ultrasound image when each scan line is created by each single transmission because the lateral intensity profiles of transmit beams significantly differ between transmissions due to a large angular interval of transmit beams (in general, the intensity is decreased by steering due to directivities of transducer elements). Such discontinuities consist of high spatial (angular) frequency components, which degrade the image quality. A simple way to reduce such discontinuities (high spatial frequency components) in an ultrasound image obtained by parallel beamforming is to use spatial moving average, i.e., low-pass filtering. Spatially averaged beamformed RF signal $\hat{O}_s(r, \theta)$ at a spatial point $\mathbf{p} = (r, \theta)$ is expressed as follows:

$$\begin{aligned} \hat{O}_s(r,\theta) &= \sum_{j=-M_s}^{M_s} w_j \cdot \hat{O}_{m0}(r, \theta + \Theta) \\ &= \sum_{j=-M_s}^{M_s} w_j \cdot \hat{O}_{m0}(r, \theta + \Theta \cdot j) \\ &\quad \cdot \exp\{-j2\pi f_\theta(\Theta \cdot j)\}|_{f_\theta=0}, \end{aligned} \tag{2.12}$$

where the number of averaging is expressed by $(2M_s + 1)$, w_j is a weighting function, and m_0 is the transmission number that gives the minimum difference between the direction of transmission $m\Theta$ and the direction θ of point $\mathbf{p} = (r, \theta)$. As can be seen in eq. (2.12), the moving average operation corresponds to the Fourier transform with respect to an angular frequency f_θ of zero. The spatial frequency spectrum obtained by eq. (2.12) is expressed by the convolution of the spatial frequency characteristics of w_j and $\hat{O}_m(r, \theta)$ and, thus, the spatial frequency characteristics of low-pass filtering by moving average operation is determined by that of the weighting function w_j. It is well known that a rectangular weighting function exhibits a higher sidelobe level in the frequency domain, which corresponds to higher leakage of high spatial frequency components. Therefore, a tapered function, such as a Hanning window, which exhibits lower sidelobe level, is preferable for weighting function w_j.

Although the high spatial frequency components can be reduced by spatial averaging, the image would be blurred because the beamformed RF signals $\{\hat{O}_m(\mathbf{p})\}$ at different spatial positions $\{\mathbf{p}\}$ are averaged in eq. (2.12). To avoid such blurring effect, in the present study, RF signals $\{\hat{O}_m(\mathbf{p})\}$ beamformed with respect to the same spatial position **p** in different transmissions $\{m\}$ are compounded. This procedure has a similar

effect given by eq. (2.12) because the lateral intensity profiles of unfocused beams, such as plane wave and diverging wave, are almost homogeneous at every angle θ within the beams. Therefore, we assumed that $\hat{O}_{m0}(r, \theta + \Theta \cdot j) \approx \hat{O}_{m0+j}(r, \theta)$.
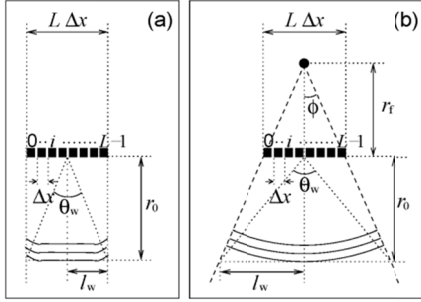

Fig. 4. Illustration of angular width θw of emitted wave. (a) Plane wave. (b) Diverging wave.

By replacing the summation with respect to angle in eq. (2.12) by that with respect to transmission, the compounded beamformed RF signal $\hat{O}_c(\mathbf{p})$ at $\mathbf{p}$ is expressed as follows:

$$\hat{O}_c(p) = \sum_{j=-M_c}^{M_c} w_{c,m0+j}(\mathbf{p}) \cdot \hat{O}_{m0+j}(\mathbf{p}), \quad (2.13)$$

where the number of compounding is expressed as $(2M_c + 1)$. In the present study, Hanning weighting was used in spatial compounding and is expressed as follows:

$$w_{c,m}(p) = \cos^2\left\{\frac{\pi}{2} \cdot \frac{(\theta - m\Theta)}{\frac{1}{2} \cdot (2M_c + 1)\Theta}\right\}, \quad (2.14)$$

where the number of compounding is expressed as $(2M_c + 1)$. In the present study, M_c was determined from the angular width of the emitted wave by considering the transducer geometry, as illustrated in Fig. 4. For plane waves, the angular width θ_w at range distance r is given by

$$\theta_w = 2\arctan\left(\frac{L \cdot \Delta x}{2r}\right). \quad (2.15)$$

For diverging waves, the diverging angle φ is obtained as follows:

$$\phi = \arctan\left(\frac{L \cdot \Delta x}{2r_f}\right). \quad (2.16)$$

In the present study, using the diverging angle φ, the lateral beam width l_w at range distance r is approximately given by

$$l_w = (r_f + r)\tan\phi. \quad (2.17)$$

The angular width θ_w for diverging wave is obtained as follows:

$$\theta_w = 2\arctan\frac{l_w}{r}. \quad (2.18)$$

The number of compounding $(2M_c + 1)$ is determined so that the contribution of the emissions, whose directions are different from the direction of interest θ by larger than half the angular beam width θ_w, are gradually decreased. In the present study, this was

given by $(2M_c + 1)\Theta/2 < \theta_w$. To satisfy this condition, the number of compounding was determined as follows:

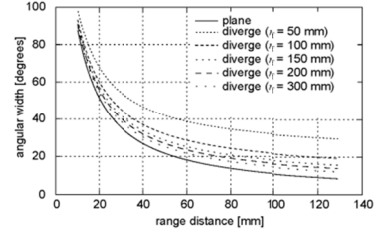$$M_c = \left\lfloor \frac{\theta_w}{\Theta} \right\rfloor. \quad (2.19)$$

Fig. 5. Angular widths {θw} calculated for plane and diverging waves.

In the present study, the angular beam width θ_w were introduced to consider the relationship between the beam width and the interval of transmit beams because sparser transmissions requires a larger beam width to illuminate a larger region between the directions of successive transmissions. The angular beam width is more convenient than the beam width in distance because the angular interval of transmit beams does not change with the range distance, whereas the interval in distance changes. In Fig. 5, angular widths {θw} calculated for plane and diverging waves using eqs. (2.15) and (2.18) are plotted as functions of range distance r (size of aperture $L \cdot \Delta x = 19.2$ mm was the same as that of the ultrasonic probe used). Angular width θ_w of a diverging wave at distance r_f of a virtual point source larger than 100 mm does not change so much compared with that of a plane wave. At the longest range distance of 130 mm, which was of interest in the present study, angular width θ_w doubles at $r_f = 100$ mm and triples at $r_f = 50$ mm. Angular width θ_w would further increase at smaller r_f. However, the intensity of the emitted wave would further decrease. Therefore, in the present study, diverging waves at $r_f = 100$ mm and 50 mm were investigated in the subsequent sections.

3. Results
3.1. Evaluation of spatial resolution using a wire phantom

In the present study, a commercial ultrasonic diagnostic system (α-10, Aloka, Tokyo, Japan) was used with a 3.75-MHz phased array probe. This system was modified so that RF echoes received by $L = 96$ individual elements could be acquired at a sampling frequency of 30 MHz for off-line processing (receive beamforming, spatial compounding, etc.).

In the basic experiment, fine nylon wires (diameter ≈ 100 μm) placed in water were used for evaluation of the spatial resolution. Figures 6(a)-(d) show B-mode images of the wires obtained by conventional sector

scanning and parallel beamforming with spatial compounding using plane waves and diverging waves at r_f = 100 mm and 50 mm, respectively. In Figs. 6(1) and 6(2), rectangular apodization ($w_{r,i}$ = 1; i = 0, 1, 2, ..., $L − 1$) and Hamming apodization ($w_{r,i}$ = 0.54−0.46 cos($2\pi i/L$); i = 0, 1, 2, ..., $L−1$) were respectively used. As can be seen in Fig. 6, the sidelobe levels significantly increased when rectangular apodization was used. Therefore, Hamming apodization was used in the subsequent experiments.
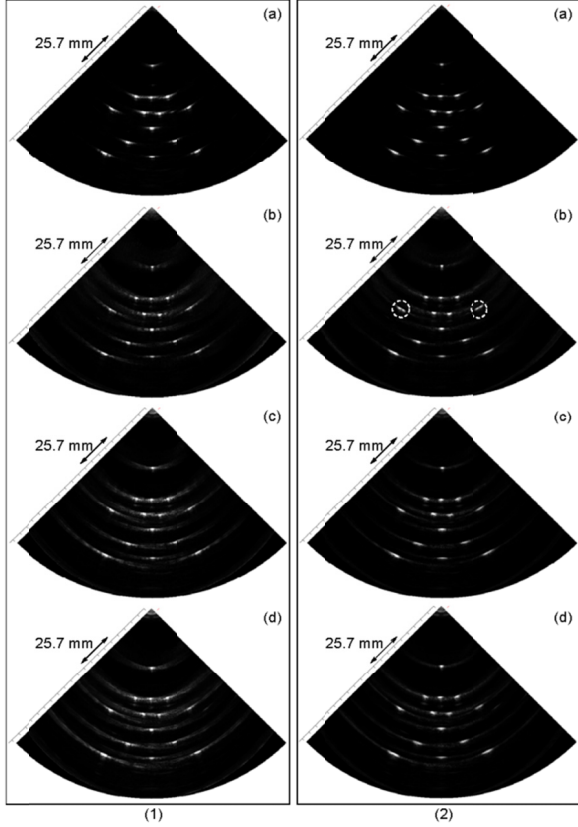
Fig. 6. B-mode images of fine wires obtained by (a) conventional sector scanning and parallel beamforming using (b) plane waves, (c) diverging waves at r_f = 100 mm, and (d) diverging waves at r_f = 50 mm. (1) Rectangular and (2) Hamming apodizations were used.

In the B-mode image obtained by parallel beamforming with plane waves, the point spread function at a larger steering angle (surrounded by white dashed lines in Fig. 6(2-b)) was distorted (split in the lateral direction) because the widths of plane waves were narrow compared with diverging waves and the widths decreased when the steering angle was increased. Therefore, the use of plane waves is limited to imaging at smaller steering angles. On the other hand, such distortion was not found in the B-mode images obtained by parallel beamforming with diverging waves.

Figures 7(a) and 7(b) show the axial and lateral profiles of the images (corresponding to point spread functions) at an angular position θ of 0 degrees and range distance r of 41 mm, respectively. The widths at half maxima of the point spread functions shown in Fig.

7 are described in table I. As shown in Fig. 7, plane wave transmission achieved the best lateral spatial resolution. Although the widths at half maxima of the point spread functions obtained by diverging waves were slightly larger than those obtained by conventional beamforming and parallel beamforming with plane waves, the point spread functions, which were very similar to that obtained by conventional beamforming could be realized by parallel beamforming with diverging beams and compounding. Figures 8(a) and 8(b) illustrate point spread functions created by compounding plane and diverging waves, respectively. The wavefronts and point spread functions shown by the dashed and solid lines illustrate those obtained by the transmission at the least steering angle and that at the maximum steering angle in beamforming with respect to spatial point **p**. The overlapping area of two point spread functions in Fig. 8 is enhanced in the resultant point spread function obtained by compounding. As can be seen in Fig. 8, the overlapping area obtained by plane waves is smaller than that obtained by diverging beams, even when the maximum steering angles are same. Therefore, it was considered that plane wave transmission achieved the best lateral spatial resolution. However, there was an increase of the lateral sidelobe level by use of parallel beamforming with both plane and diverging waves. Although this increase of the sidelobe level would degrade the image contrast, the lateral spatial resolution comparable to that of conventional sector scan was achieved by the proposed method.
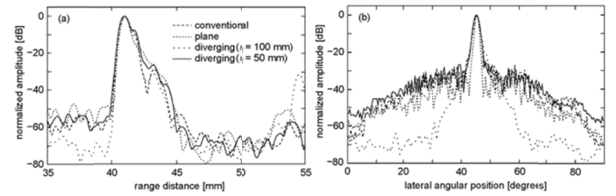

Fig. 7. Axial and lateral profiles of envelopes of beamformed RF echoes obtained by respective methods. (a) Axial profile at a lateral angular position of 0 degrees. (b) Lateral profile at a range distance of 41 mm.
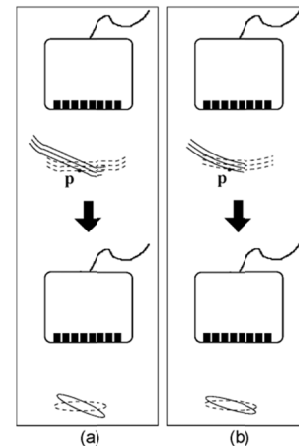

Fig. 8. Wavefronts and point spread functions produced by (a) plane waves and (b) diverging waves.

	conventional beamforming	plane wave	diverging wave ($r_f = 100$ mm)	diverging wave ($r_f = 50$ mm)
axial [mm]	0.73	0.71	0.88	0.84
lateral [mm]	0.68	0.52	0.81	0.86

Table 1. Widths at half maxima of point spread functions shown in Fig. 7.

In Fig. 7, the number of compounding ($2M_c + 1$) was determined by eq. (2.19). In Fig. 9(1) and 9(2), M_c was also determined by eq. (2.19), however, the maximum of M_c was limited to be 4 and 2, respectively. For diverging waves, B-mode images obtained by limiting the maximum number of compounding were better than those obtained with unlimited M_c, as shown in Fig. 6. In the present study, the propagation delay of the emitted wave was calculated based on eq. (2.8) without considering the distortion of wavefront due to beam steering. Therefore, it can be considered that the number of compounding M_c larger than 2 (corresponding to larger differences among the steering angles in emissions used for compounding) degraded the resultant images because it would be difficult to estimate propagation delays at larger steering angles by eq. (2.8) and the large number of transmissions (means a large difference among the angles of transmissions) used for compounding degrades coherent compounding. As in Fig. 7, Fig. 10 shows lateral profiles of envelopes of compounded beamformed RF echoes at a range distance of 41 mm obtained by a diverging beam at $r_f = 50$ mm with and without limitation of $M_c \leq 2$. In Fig. 10, only the profiles obtained with a diverging beam at $r_f = 50$ mm are shown because the number of compounding is largest among the transmit beams used in the present study. As shown in Fig. 10, degradation of coherent compounding reduces the difference between the main lobe and sidelobe levels and does not improve the spatial resolution. Consequently, in the present study, the number of compounding ($2M_c + 1$) was determined by eq. (2.19); however, its maximum was restricted to be 5 for diverging waves.

In general, the insonified energy of a diverging wave spreads and acoustic intensity decreases with propagation distance. To reduce this decay, in the present study, the width of the diverging beam was limited. Figure 11 shows the axial profiles of the ultrasound images of the wire phantom (shown in Fig. 6) at a lateral angle of 0 degrees. As expected, the intensity at the deepest wire was strongest when focusing was done in both transmit and receive, as shown in Fig. 11. Although the intensity was lower than that obtained by focusing in both transmit and receive, the diverging waves used in the present study achieved decays of intensities (Figs. 11(c) and 11(d)) which were similar to that realized by plane waves (Fig. 11(b)).
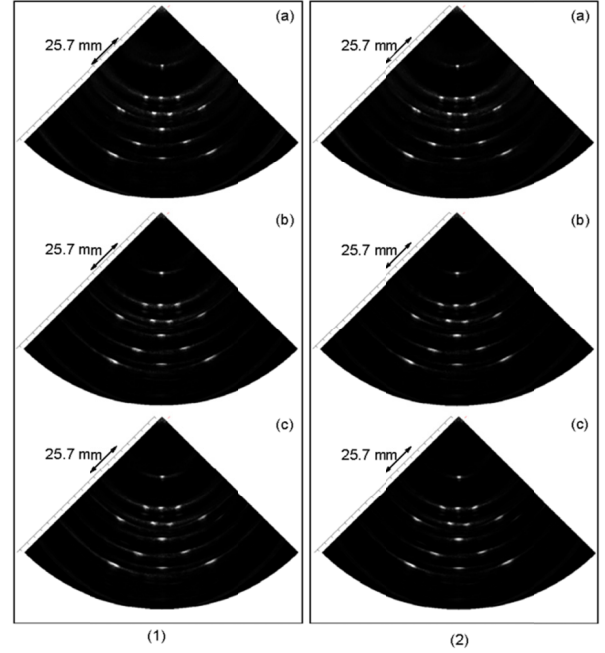

Fig. 9. B-mode images of fine wires obtained by parallel beamforming with (a) plane waves, (b) diverging waves at rf = 100 mm, and (c) diverging waves at rf = 50 mm. Maxima of the number of compounding were limited to be (1) 4 and (2) 2.
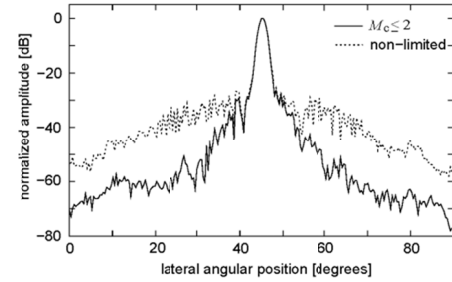

Fig. 10. Lateral profiles of envelopes of beamformed RF echoes at a range distance of 41 mm obtained by a diverging beam at $r_f = 50$ mm with and without limitation of $M_c \leq 2$.

3.2 *In Vivo* Imaging of a Human Heart

Figure 12(a)-(d) shows B-mode images of the heart of a 23-year-old healthy male obtained by conventional sector scan and parallel beamforming with plane waves and diverging waves at $r_f = 50$ mm and 100 mm, respectively. The maximum of the number of compounding M_c was limited to 2 for diverging waves. Although a B-mode image of a heart could be obtained by plane wave transmission, the point spread function produced by parallel beamforming with plane waves were split in the lateral direction, as shown in Fig. 6. Therefore, it might be better to use plane wave transmission with a smaller maximum steering angle. By using diverging waves, as shown in Figs. 12(c) and 12(d), B-mode images of the heart could be obtained at a high frame rate of 316 Hz with a full lateral field of view of 90 degrees, and the diverging waves at $r_f = 50$

mm and 100 mm showed similar performances. Although the image contrast were degraded due to the higher lateral sidelobe levels, a B-mode image, whose image quality was comparable to that obtained by conventional sector scanning, could be obtained at a frame rate (316 Hz) significantly higher than that (39 Hz) obtained by conventional sector scan, and a full field of view of 90 degrees was achieved without requiring ECG gating [11].
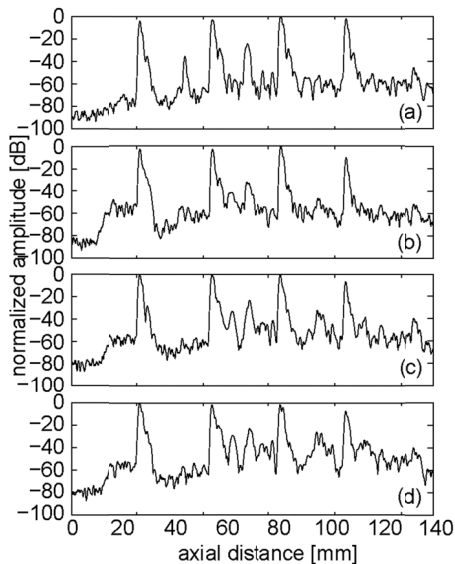

Fig. 11. Axial profiles of the images of wires (shown in Fig. 6) at a lateral angle of 0 degrees. (a) Conventional beamforming (focusing in both transmit and receive). (b) Parallel beamforming with plane waves. (c) and (d) Parallel beamforming with diverging beams at $r_f = 100$ mm and 50 mm, respectively.

4. Discussion

In the present study, a method based on parallel beamforming was investigated for high frame rate echocardiography. To realize B-mode imaging in a sector format based on parallel beamforming, spherically diverging waves were used in transmission.

In the present study, in receive beamforming, the propagation delay of the emitted diverging wave was calculated by considering the geometry of the transducer array and the virtual point source. However, the increase of the number of compounding M_c, which corresponds to the increase of the transmission steering angle from the direction of interest θ, degraded the resultant B-mode images. This would be caused by the distortion of the wavefront of the emitted wave due to steering. In future work, methods for accurate realization of the desired wavefront or accurate calculation of the resultant wavefront will be necessary to increase the number of compounding for further improvements of the image resolution because the difference in angles of wavefronts in different transmissions would increase by using more number of transmissions for compounding, as illustrated in Fig. 8.

In addition, phase aberration correction [26,27] would be useful for receive beamforming.
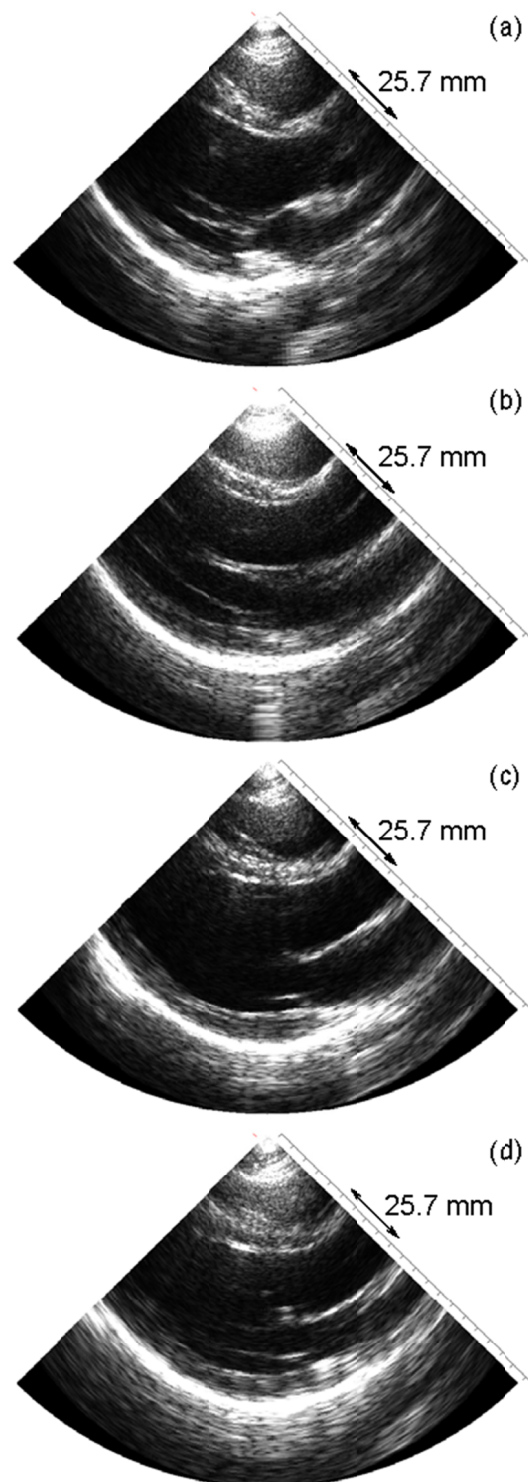

Fig. 12. B-mode images of a heart of a 23-year-old healthy male obtained by (a) conventional sector scanning and parallel beamforming using (b) plane waves, (c) diverging waves at rf = 100 mm, and (d) diverging waves at $r_f = 50$ mm. The maximum number of compounding was limited to be 2 for diverging waves.

Although diverging waves should be used to achieve a full lateral field of view of 90 degrees, plane waves could be used for imaging of a narrower region. Plane waves are more easily implemented in ultrasonic diagnostic equipment and make it easier to calculate the propagation delay of the wavefront. This was shown by the results in Fig. 9 that the increase of the maximum number of compounding did not degrade the resultant B-mode image in the case of plane wave transmission. The error in the calculated propagation delay at larger steering angles was considered to be smaller for plane waves than for diverging waves. Figure 13 shows a longitudinal B-mode image of the heart of the same subject as in Fig. 12 obtained with plane wave transmission and smaller steering angles. As can be seen in Fig. 13, a B-mode image of good quality can be obtained at a very high frame rate (1010 Hz) that is much higher than that (200 Hz) achieved by conventional sector scanning with a narrow field of view [10].
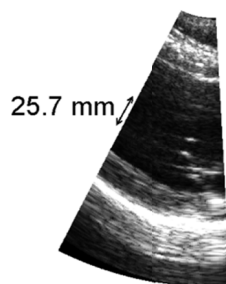

Fig. 13. B-mode image of the heart of the same subject as in Fig. 12 obtained by parallel beamforming with plane waves and a smaller maximum steering angle (frame rate: 1010 Hz).

The limitation of the current hardware used in the present study is that it takes about 1 minute to prepare for transmission of diverging waves. During this preparation, an operator needs to fix the position of the ultrasonic probe without viewing B-mode images. This limitation significantly increases the difficulties of in vivo measurements, particularly scanning of the same section several times. In future work, we need to develop a real-time system realizing the method proposed in the present study.

5. Conclusion

In this study, methods for measurement of viscoelasticity of arterial wall and evaluation of red blood cell aggregation were developed. Such methods would be useful for early diagnosis of atherosclerosis.

References

[1] Sutherland GR, Salvo GD, Claus P, et al. Strain and strain rate imaging: A new approach to quantifying regional myocardial function. *J Amer Soc Echocardiogr* **17**, 788–802, 2004.

[2] Sutherland GR, Stewart MJ, Groundstroem KW, et al. Color Doppler myocardial imaging: A new technique for the assessment of myocardial function. *J Amer Soc Echocardiogr* **7**, 441–458, 1994.

[3] Heimdal A, Støylen A, Torp H, et al.Real-time strain rate imaging of the left ventricle by ultrasound. *J Amer Soc Echocardiogr* **11**, 1013–1019, 1998.

[4] Yoshiara H, Hasegawa H, Kanai H, et al. Ultrasonic imaging of propagation of contraction and relaxation in the heart walls at high temporal resolution. *Jpn J Appl Phys* **46**, 4889–4896, 2007.

[5] Kanai H. Propagation of spontaneously actuated pulsive vibration in human heart wall and in vivo viscoelasticity estimation. *IEEE Trans Ultrason Ferroelectr Freq Control* **51**, 1931–1942, 2005.

[6] Kanai H. Propagation of vibration caused by electrical excitation in the normal human heart. *Ultrasound Med Biol* **35**, 936–948, 2009.

[7] Bers DM. *Excitation-contraction coupling and cardiac contractile force, 2nd ed.* Dordrecht: Kluwer Academic Publishers, 2001.

[8] Konofagou E, Luo J, Fujikura K, et al. Imaging the electromechanical wave imaging of cardiovascular tissue *in vivo*. *Proc IEEE Ultrasonics Symp*, 985–8, 2006.

[9] Konofagou EE, D'hooge J, Ophir J. Myocardial elastography–A feasibility study *in vivo*. *Ultrasound Med Biol* **28**, 475–482, 2002.

[10] D'hooge J, Konofagou E, Jamal F, et al. Two-dimensional ultrasonic strain rate measurement of the human heart *in vivo*. *IEEE Trans Ultrason Ferroelectr Freq Control* **49**, 281–286, 2002.

[11] Wang S, Lee W, Provost J, et al. A composite high-frame-rate system for clinical cardiovascular imaging. *IEEE Trans Ultrason Ferroelectr Freq Control* **55**, 2221-2233, 2008.

[12] Kanai H, Koiwa Y. Myocardial rapid velocity distribution. *Ultrasound Med Biol* **27**, 481–498, 2001.

[13] Bradley C. Retrospective transmit beamformation. *Whitepaper ACUSON SC2000TM Volume Imaging Ultrasound System*, 2008.

[14] Lu J. 2D and 3D high frame rate imaging with limited diffraction beams. *IEEE Trans Ultrason Ferroelectr Freq Control* **44**,839–856, 1997.

[15] Lu J. Experimental study of high frame rate imaging with limited diffraction beams. *IEEE Trans Ultrason Ferroelectr Freq Control* **45**, 84–97, 1998.

[16] Cheng J, Lu J. Extended high-frame rate imaging method with limited-diffraction beams. *IEEE Trans Ultrason Ferroelectr Freq Control* **53**, 880–899, 2006.

[17] Lu J, Cheng J, Wang J. High frame rate imaging system for limited diffraction array beam imaging with square-wave aperture weightings. *IEEE Trans Ultrason Ferroelectr Freq Control* **53**, 1796–1812, 2006.

[18] Shattuck DP, Weinshenker MD, Smith SW. Explososcan: A parallel processing technique for high speed ultrasound imaging with linear phased arrays. *J Acoust Soc Amer* **75**, 1273–1282, 1984.

[19] Tanter M, Bercoff J, Sandrin L, et al. Ultrafast compound imaging for 2-D motion vector estimation: Application to transient elastography. *IEEE Trans*

Ultrason Ferroelectr Freq Control **49**, 1363–1374, 2002.

[20] Hasegawa H, Kanai H. Simultaneous imaging of artery-wall strain and blood flow by high frame rate acquisition of RF signals. *IEEE Trans Ultrason Ferroelectr Freq Control* **55**, 2626–2639, 2008.

[21] O'Donnell M, Thomas LJ. Efficient synthetic aperture imaging from a circular aperture with possible application to catheter-based imaging. *IEEE Trans Ultrason Ferroelectr Freq Control* **39**, 360-380, 1992.

[22] Karaman M, O'Donnell M. Synthetic aperture imaging for small scale systems. *IEEE Trans Ultrason Ferroelectr Freq Control* **42**, 429–442, 1995.

[23] Hasegawa H, Kanai H.Fast ultrasonic imaging of the heart using spherically diverging beam. *Technical Report of IEICE* **110**(171), 65–68, 2010.

[24] Mahafza BR. *Introduction to radar analysis*. Boca Raton: CRC Press; 1998.

[25] Jespersen SK, Wilhjelm JE, Sillesen H. Multi-angle compound imaging. *Ultrason Imaging* **20**, 81–102, 1998.

[26] Fortes JMP. A closed loop ML algorithm for phase aberration correction n phased array imaging systems–Part I: Algorithm synthesis and experimental results. IEEE Trans *Ultrason Ferroelectr Freq Control* **44**, 259–270, 1997.

[27] Li Y. Phase aberration correction using near-field signal redundancy–Part I: Principles. *IEEE Trans Ultrason Ferroelectr Freq Control* **44**, 355–371, 1997.